Surface & Coatings Technology xxx (2016) xxx–xxx

Contents lists available at ScienceDirect

Surface & Coatings Technology

journal homepage: www.elsevier.com/locate/surfcoat

Influence of the surface chemistry-structure relationship on the nanoscale friction of nitrided and post-oxidized iron

Caren M. Menezes [a,*], Nério Bogoni Jr. [a], Jenifer Barrirero [b], Hisham Aboulfadl [b], Frank Mücklich [b], Carlos A. Figueroa [a]

[a] Centro de Ciências Exatas e Tecnologia, Universidade de Caxias do Sul, Caxias do Sul, RS 95070-560, Brazil
[b] Chair of Functional Materials, Campus D3 3, Saarland University, D-66123 Saarbrücken, Germany

ARTICLE INFO

Article history:
Received 2 April 2016
Revised 12 July 2016
Accepted in revised form 14 July 2016
Available online xxxx

Keywords:
Nanoscale friction
Surface chemistry
Phase distribution
Iron
Oxide
Nitride

ABSTRACT

The relationship between the friction behavior and surface properties such as surface chemistry, morphology and phase distribution is not fully understood. In the case of surface treatments involving steels, the alloying elements introduce non-controllable variables in tribological experiments. We further advance this discussion by designing experiments where the friction behavior of a conical diamond tip sliding on different plasma nitrided and post-oxidized pure iron substrates was determined. Also, a detailed chemical and microstructural surface characterization using discharge optical emission spectroscopy, X-ray diffraction, and atom probe tomography was performed. Implementing composition profiling and localized elemental distribution analysis throughout the outermost layer, the formation of iron oxide with non-homogenous morphology was detected. Although the coefficient of friction decreases as a function of the post-oxidation time, the friction force is under a relative great dispersion at intermediate post-oxidation times. The dispersion of the friction force obtained from the sliding analyses can be understood as a combination of surface chemistry and different phases (structure) at the surface.

1. Introduction

The sustainability of Earth is a driving force enabling cutting-edge technologies that can avoid or reduce the environmental impact of several current contaminant processes. Moreover, less-energy consuming alternatives are a crucial point for defining the political agenda in both public and private sectors. In particular, mechanical and electromechanical devices can save energy by eliminating or reducing the friction forces, which are present due to the physical contact of different moving parts [1]. Despite of huge effort in interpreting the nature of friction forces, its fundamental meaning remains open from Leonardo da Vinci's experiments.

Nowadays, for both macroscopic and microscopic surfaces there is a well-established understanding of the friction phenomenon under the view of phenomenological laws, which are based mostly on the theory of mechanical contact [2]. However, a complete understanding of the friction coefficient of two surfaces in relative motion must focus the physical phenomena that are taking place at the nanoscale.

The understanding of chemical and physical phenomena related to the friction at the nanoscale is gaining more attention in tribology [3–5]. Several fundamental contributions and nanoscale aspects of the phenomenological friction coefficient have been recently pointed out in theories that are based on phononic and electronic mechanisms [6]. Moreover, new phenomena are including friction anisotropy [7], tribocharges [4], magnetic effects [3,8], superlubricity [9], and also the dependence on the sliding velocity [10]. Most of these fundamental phenomena are related to processes such as phonon excitation, electrostatic attraction/repulsion, and electronic effects that contribute to the energy dissipation associated with non-conservative friction forces [6]. A common interest in the tribology community aiming at the nanoscopic interpretation of friction is to perform controlled experiments where friction mechanisms at the atomic level can be split off from micro and macroscopic contributions. However, several works related to the origin of friction at the nanoscale are still controversial [11].

Surface chemistry has also been invoked to explain the friction behavior of different surfaces. Indeed, the charge-to-ratio relationship controls the friction behavior of several oxides [12]. Recently, the decrease of the coefficient of friction due to the replacement of nitrogen by oxygen atoms in nitrided AISI 1045 steel was explained by phononic models [13]. However, the surface structure and morphology must also be taken into account to understand the friction behavior as a whole. Although the influence of morphology on the coefficient of friction is mainly though in terms of surface roughness [14], the mechanical properties of material phases that constitute the surface play also a crucial role [15].

In the case of oxidized steels, some controversies were recently published. The rolling reduction of rolls made from different stainless steels

* Corresponding author.
E-mail address: engcaren@hotmail.com (C.M. Menezes).

http://dx.doi.org/10.1016/j.surfcoat.2016.07.095
0257-8972/

shows a contrary behavior when the rolls are oxidized [16]. Moreover, the oxide layer of the AISI 430 oxidized steel is easily removed and the combination of chromium oxide and iron oxide (two different phases) increases the friction of coefficient [16]. Therefore, these results could be interpreted by taking into account not only the surface chemistry and roughness but also the phase distribution at the surface. Moreover, the alloying elements of steels may introduce non-controllable effects.

In this context, the aim of this work is assessing the effect of surface chemistry and structure on the frictional behavior of the outermost layers in nitrided and post-oxidized pure iron substrates. In order to avoid the undesirable effect of alloying elements in the analyzed properties, we have used pure iron in our experiments.

2. Experimental

Samples were cut from a 12 mm diameter pure iron (nominal composition of 99,99%) bar. The substrates were mirror polished with colloidal silica by standard metallographic techniques. Plasma nitriding and post-oxidizing were performed in a laboratory scale chamber (base pressure ≤ 1.8 Pa). For plasma nitriding, a gaseous mixture of 89% N_2 and 11% H_2 was injected into the chamber by using mass flow controllers and the working pressure was fixed at 1 mbar. During this step, the working temperature was kept at 550 ± 3 °C for 5 h. An applied voltage of 770 ± 20 V and current density of 1.2 mA·cm^{-2} with a frequency of 10 kHz and a duty cycle of 25% were provided from a pulsed power supply (CVD Valle 4000). Following the plasma nitriding process, a subsequent post-oxidation process was performed in the same chamber, without any contact to the external atmosphere. A set of five samples was processed. The first sample was nitrided only while the others four samples were nitrided and post-oxidized during 30, 60, 180, and 300 s, respectively, at a constant temperature of 480 ± 4 °C. The post-oxidizing gaseous mixture was constituted of 70% N_2, 20% H_2, and 10% O_2 and the working pressure was kept at 2.5 mbar. In this step, an applied voltage of 700 V ± 20 V and current density of 2.0 mA·cm^{-2} with a frequency of 10 kHz and a duty cycle of 25% were provided from the same pulsed power supply.

A diffractometer Shimadzu XRD-6000 equipped with a Cu tube that uses the Kα line (V = 40 kV and I = 30 mA) was employed to identify the crystalline structure of the plasma-modified outermost layers. The experiments were conducted at grazing angle incidence (θ = 2°). Samples were rotated with constant velocity around the vertical axis during analysis in order to reduce preferential orientation and textural effects.

Glow discharge optical emission spectroscopy (GD-OES, Horiba, GD Profiler 2) was used to obtain the qualitative chemical profile of the modified surfaces by measuring the emission intensities of chemical elements. The measurements were performed at 630 Pa and 30 W, during an acquisition time of 120 s.

The atom probe tomography (APT) analysis were carried out using a CAMECA™ LEAP 3000× HR system in laser pulsing mode (532 nm wavelength), at a repetition rate of 100 kHz and a specimen temperature of about 60 K. Laser pulse energy of 0.3 nJ was used for the nitrided sample, and 1.0 nJ was used for the post oxidized samples (30 and 60 s). In order to preserve the region of interest along the surface, a 50 nm thick titanium-capping layer was deposited on top of the samples by physical vapor deposition. Site-specific sample preparations were afterwards prepared in a dual beam focused ion beam/scanning electron microscopy workstation (FIB/SEM) (Helios NanoLab 600™, FEI Company, USA). APT datasets were reconstructed and analyzed with the CAMECA™ IVAS 3.6.8 software.

The friction measurements were carried out in sliding mode using a NanoTest-600 equipment (MicroMaterials Ltd) where a conical diamond indenter with a final radius of 25 μm was used to inspect the surfaces. In our experiments, different normal loads of 1, 2, 5, 10, 15, and 20 mN were applied and the samples were displaced at a rate of 1 μm·s^{-1} up to a total distance of 680 μm. The tangential force was measured and its average steady-state value was correlated with the applied normal force on the functionalized surfaces in order to obtain the coefficient of friction (CoF).

3. Results and discussion

3.1. Crystalline structure and qualitative chemical profiles

The X-ray diffraction patterns at grazing angle (θ = 2°) obtained from the nitrided and post-oxidized samples are shown in Fig. 1. Considering the grazing angle and the material type, the information of the diffraction experiments is about 800 nm in-depth. According to the diffraction patterns, all samples are displaying a mixture of iron nitride phases, mainly γ′-Fe_4N (PDF database: 00–001-1219) and ε-$Fe_{2-3}N$ (PDF database: 00-001-1236). Besides this, only one type of iron oxide, i.e., Fe_3O_4 (PDF database: 00-001-1111) was formed during the plasma post-oxidizing step.

Figs. 2 (a) and (b) show the qualitative oxygen and nitrogen chemical profiles, respectively, for all samples measured by GD-OES. One can see that the oxygen content increases with the increasing of the post-oxidizing time. Although the post-oxidized samples during 30 s and 60 s have shown similar oxide layer thicknesses, the post-oxidized sample at the longest time (300 s) exhibits the thickest oxide layer. Furthermore, a slight oxygen signal was recorded in the nitrided-only sample and in pure iron, which could be related to atmospheric oxygen physisorption and was also reported in other studies under the same circumstances [13]. It is evident that the nitrogen signal becomes lower in a broader depth at longer post-oxidizing times, which is self-consistent with the oxygen signal (see Fig. 2b). Albeit the outermost layer is mainly constituted by magnetite (iron oxide), nitrogen atoms seem to be present in such outermost layer, forming a transition zone with a mixture of iron nitrides and magnetite. Moreover, the oxide layer thickness does not follow a square root law with the post-oxidation time, indicating a physicochemical process that is being controlled by a reaction-diffusion mechanism where oxygen reacts with iron nitride and promotes diffusion [17].

3.2. Friction behavior

The coefficients of friction (CoF) versus sliding distance for the nitrided sample and the post-oxidized samples for 60 s and 300 s at a fixed normal load of 10 mN are shown in Fig. 3. From the mean value it is possible to observe a decrease in the CoF for the post-oxidized samples compared with the nitrided sample. However, a different dispersion was identified during the sliding progress as a whole. From that, the coefficient of variance (CoV) was calculated and compared among samples. While the nitrided-only sample exhibits the lowest CoV, the post-oxidized sample during 60 s shows the highest dispersion. However, this dispersion falls down at longer post-oxidation times, as observed in the post-oxidized sample for 300 s (see Fig. 3).

3.3. Quantitative chemical inspection by atom probe analysis (APT)

The APT analysis was implemented to measure the thickness, composition, and distribution of the oxide layer formed in the two post-oxidized samples during 30 and 60 s and to compare them to the nitrided sample, which was used as reference. The nitrided-only sample showed oxides by up to about 30 nm in-depth that penetrated into the nitrided layer along localized regions, as shown in Fig. 4a. Isoconcentration surface for oxygen is used to highlight the oxide distribution below the surface (see Fig. 4b).

Fig. 4c shows a proximity histogram (proxigram) presenting a profile across the oxide-nitride layer interface for the nitrided-only sample. Within the oxidized region contents of about 26 at.% of oxygen and 5 at.% of nitrogen were detected which indicates a contamination by atmospheric oxygen due to physisorption that occurred after the plasma nitriding process. Moreover, the nitrided layer exhibits about 10 at.% of nitrogen, which is in good agreement with the GD-OES results.

Please cite this article as: C.M. Menezes, et al., Surf. Coat. Technol. (2016), http://dx.doi.org/10.1016/j.surfcoat.2016.07.095

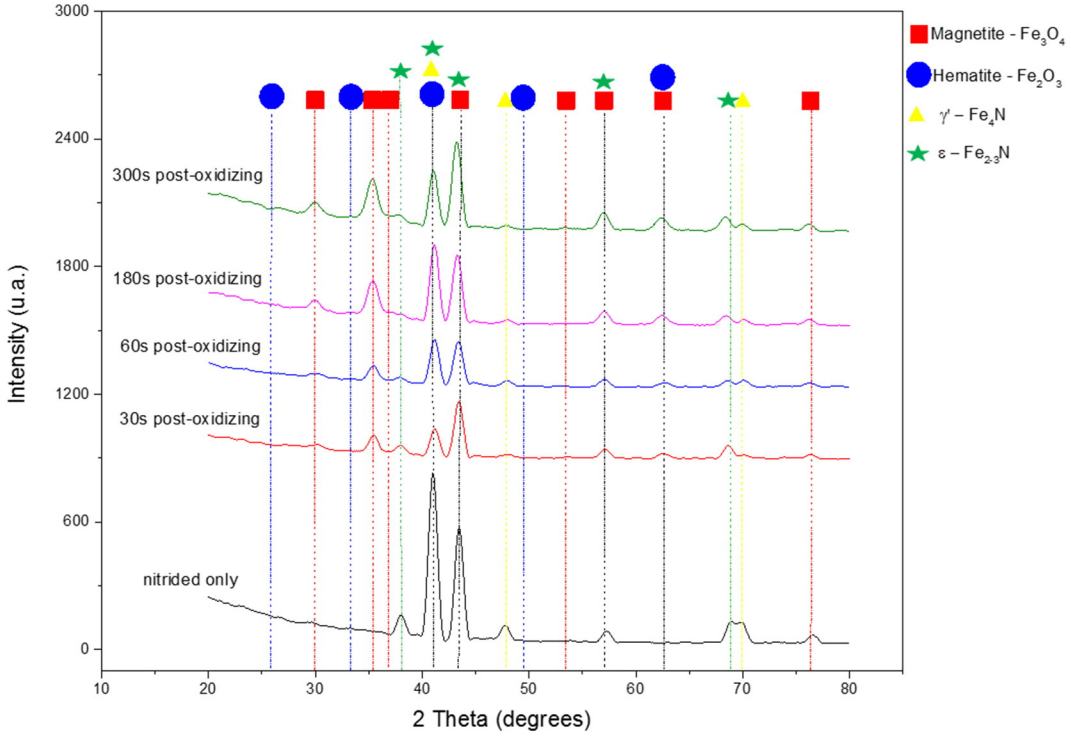

Fig. 1. X-ray diffraction patterns obtained from the nitrided only and nitrided and post-oxidized samples for different post-oxidation times of 30, 60, 180, 300 s.

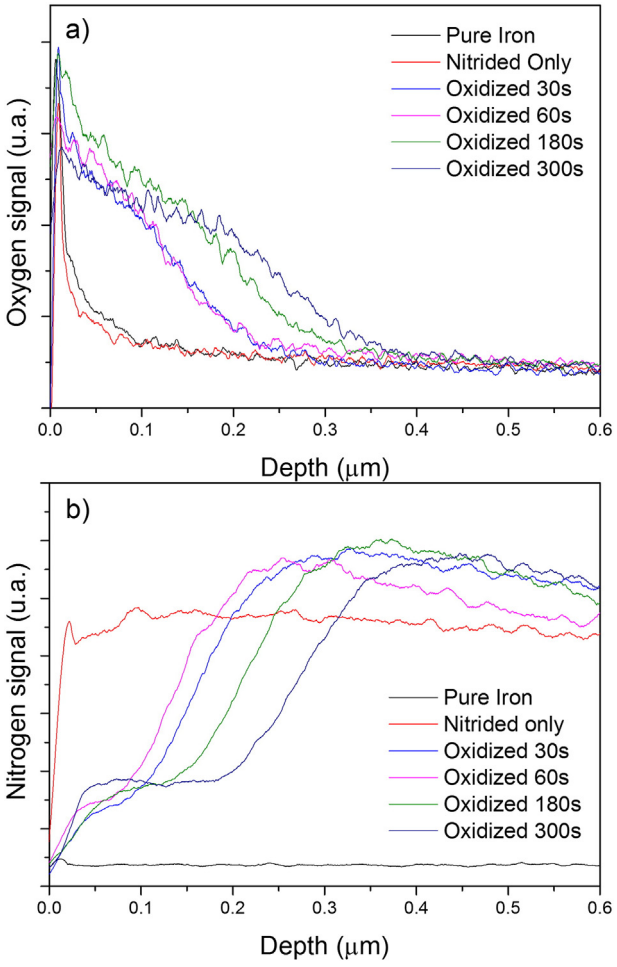

Fig. 2. (a) and (b) Qualitative oxygen and nitrogen chemical profiles, respectively, obtained by GDOES for all the functionalized samples.

The APT reconstruction of the post-oxidized sample during 60 s shows an oxide thickness that extends up to 120 nm (see Fig. 5a). Moreover, the oxide layer seems to be non-homogeneous when the depth axis is considered. Indeed, iron oxide coexists with iron nitride at the same depth. The same behavior was observed for the post-oxidized sample during 30 s with a non-homogenous oxide layer that extends up to 100 nm in-depth (not shown). Furthermore, the oxygen content was similar for both post-oxidized samples (30 and 60 s) and the value of about 44 at.% of oxygen roughly fits the magnetite stoichiometry (Fe_3O_4). Fig. 5b shows a proximity histogram (proxigram) presenting a profile across the oxide-nitride layer interface where the nitrogen and oxygen concentrations are detailed for the post-oxidized sample during 60s. One can conclude that the outermost layer of both post-oxidized samples during 30 and 60 s has a mixture of phases (iron oxide and nitride).

3.4. Chemical - structure relationship on friction behavior

Fig. 6 shows the arithmetic mean of the CoF for five independent measurements as a function of the applied normal load for all samples. As above discussed, the CoF of the nitrided-only is higher than the post-oxidized samples. One can see that in all cases the CoF stabilizes when normal loads higher than 10 mN were applied. Moreover, the CoF depends on the post-oxidation time, yielding a lower CoF at longer post-oxidation times.

Despite phononic models predict that the CoF depends strongly on the presence of different chemical structures [5,13], the high coefficient of variance (CoV) of the CoF observed at intermediate post-oxidation times (30 and60s) should be more related to surface structure characteristics than chemical aspects. These evidences are supported from the APT results. This structural evaluation indicates a phase transition when the surface is partially covered by magnetite at intermediate post-oxidation times. In fact, the kinetic of the oxide formation controls the phase distribution leading to a gradual change of the surface structure. Such a phase transition introduces non-homogeneities that augment the CoF dispersion at intermediate post-oxidation times.

Please cite this article as: C.M. Menezes, et al., Surf. Coat. Technol. (2016), http://dx.doi.org/10.1016/j.surfcoat.2016.07.095

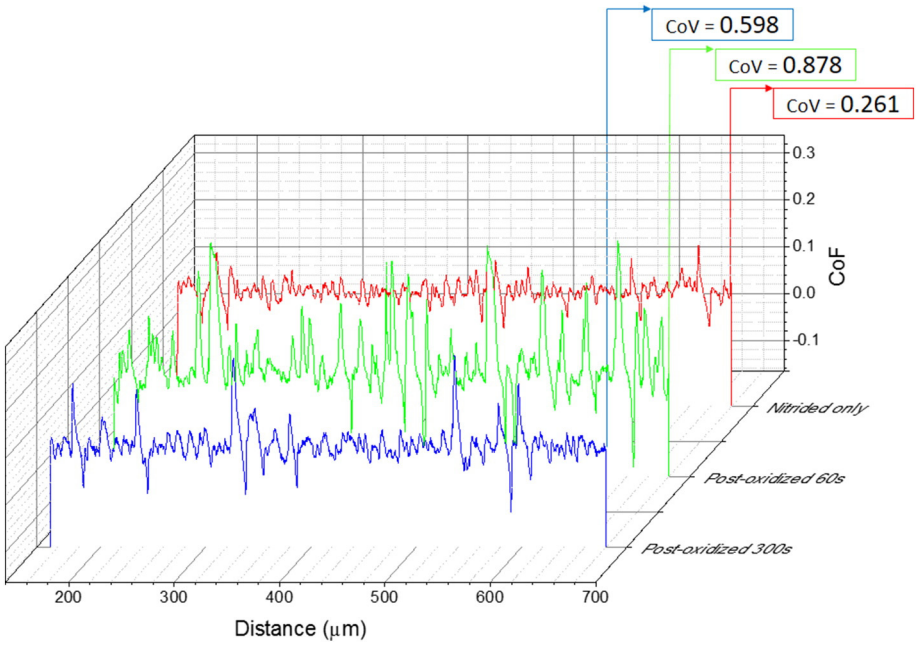

Fig. 3. The coefficients of friction versus sliding distance for 3 different samples at a fixed normal load of 10 mN. The coefficients of variance (CoV) are also shown.

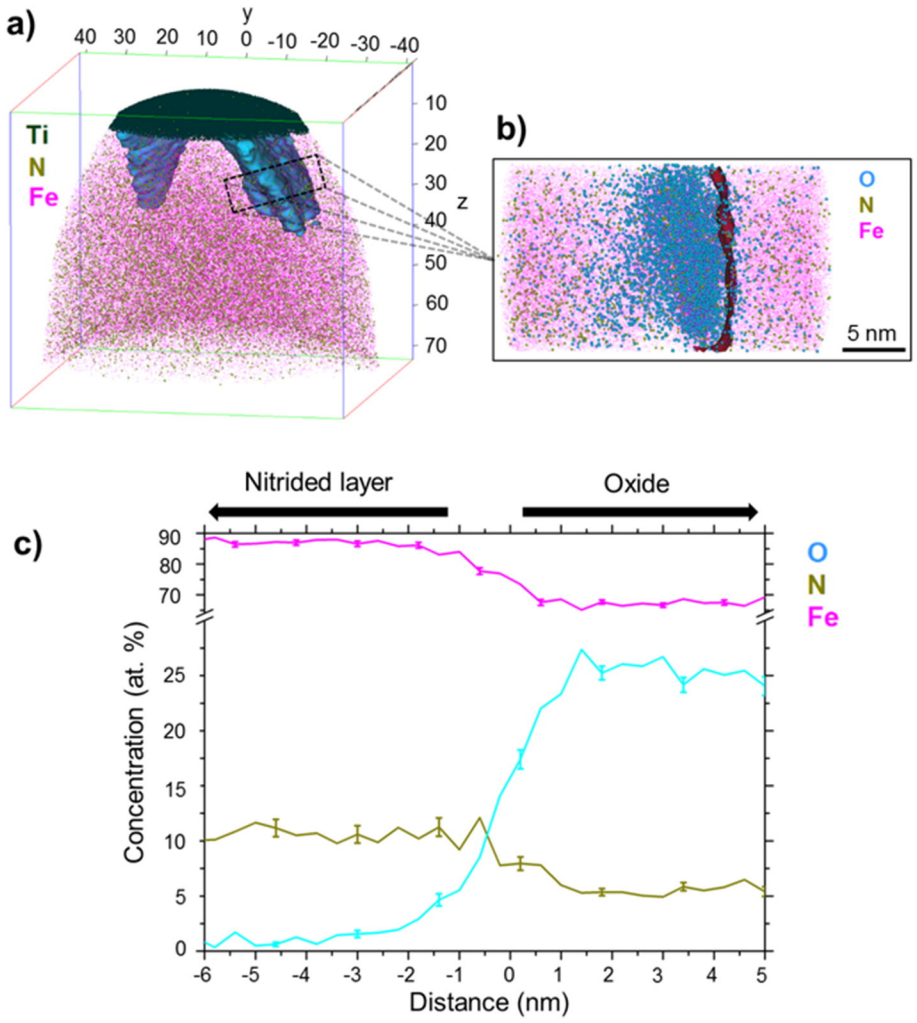

Fig. 4. APT analysis of the nitride sample. (a) 3D reconstruction with 5 at.% O isoconcentration surface (blue). Elements are represented with different atom sizes for visualization purposes. (b) The localized volume along the oxide (marked in (a)) with 18 at.% O isoconcentration surface displayed along one side of the oxide layer. (c) Proxigram profile analysis of an isolated oxide (residual oxygen from the atmosphere) on the nitided layer. (For interpretation of the references to color in this figure legend, the reader is referred to the web version of this article.)

Please cite this article as: C.M. Menezes, et al., Surf. Coat. Technol. (2016), http://dx.doi.org/10.1016/j.surfcoat.2016.07.095

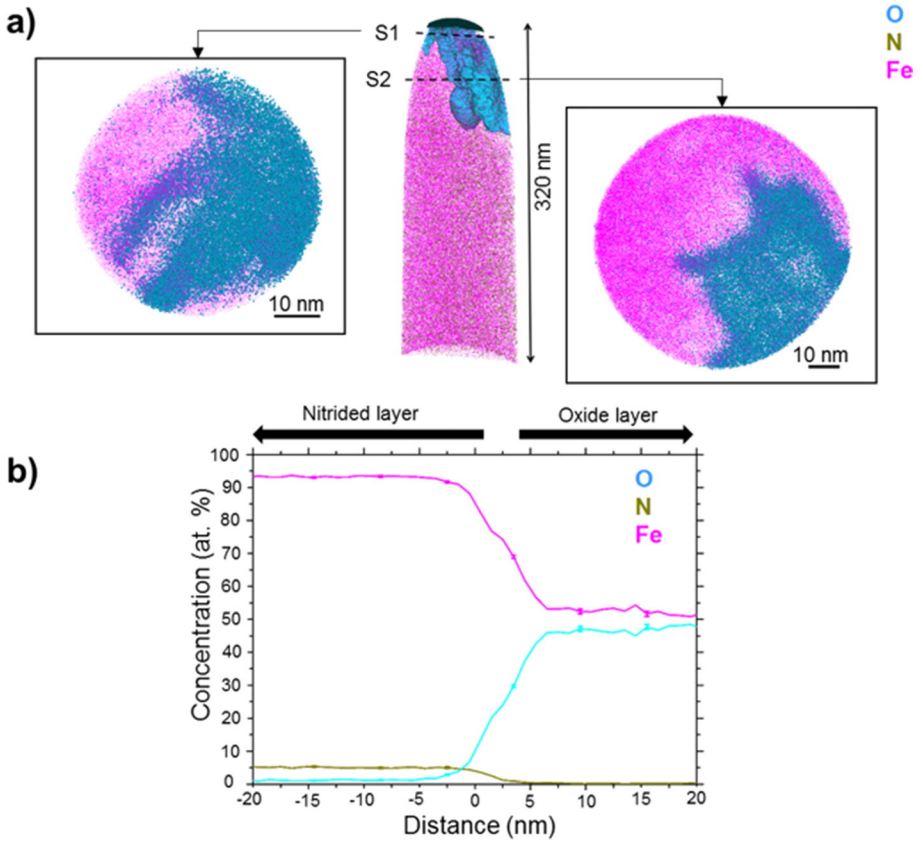

Fig. 5. (a) APT analysis of the sample post-oxidized during 60 s. The insets show two tomographic slices at different depths marked as S1 and S2, respectively (N atoms not shown). (b) Proxigram profile analyses of the sample post-oxidized during 60 s at the nitride/oxide interface.

For the sake of clarity, Fig. 7 shows a schematic of the diamond tip that slides on the modified surfaces with three different composition. The coefficients of friction and variance are also shown. Even though dispersion (CoV) is greater in the post-oxidized samples at intermediate times, the CoF is reduced when surface is covered by iron oxide. The presence of a mixture of phase at the surface is augmenting the dispersion of the CoF and the decrease of the CoF could be attributed to the lubricious property of oxides as well known in tribology applications and even explained by phononic models. Furthermore, our results reveal the importance of the surface chemistry structure relationship for explaining both the CoF and its dispersion of a tribological system. Such a relationship of chemical species, surface morphology and phase distribution could be used to understand the energy dissipation mechanisms involving non-conservative forces.

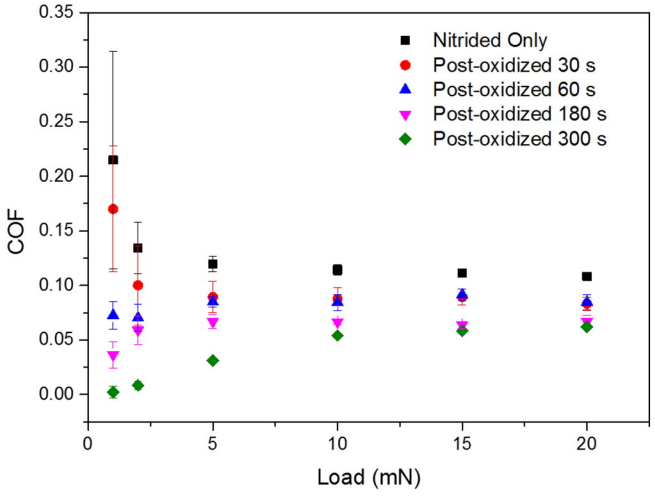

Fig. 6. Friction coefficient versus normal load for different nitrided and post-oxidzed samples.

4. Conclusion

Pure iron samples were plasma nitrided and post-oxidized during different post-oxidation times from 30s to 300 s. The modified surfaces are constituted by iron nitrides (γ'-Fe_4N and ε-$Fe_{2-3}N$) and magnetite (Fe_3O_4). Chemical profile analysis allows determination that the outermost layer of the post-oxidized samples is mainly formed by magnetite and residual nitrogen atoms. The microstructural investigation revealed that the post-oxidation process does not induce the formation of a homogenous oxide layer for the post-oxidized samples during 30s and 60s (intermediate times). Although, the coefficient of friction decreased as a function of the post-oxidation time, the biggest dispersion of the CoF was noticed at intermediate post-oxidation times. From the microstructural and chemical analysis, one can relate the non-homogeneous growth of the oxide on surface (mixture of phases) with the biggest dispersion of the CoF. In conclusion, the chemical and structural atomic information about the constitution and phase distribution at the surface must be taken into account to understand not only the CoF behavior but also the dispersion of the COF in a material system.

Acknowledgments

The authors are grateful to UCS, INCT-INES (CNPq - #554336/2010-3), CAPES, FAPERGS (0364-2551/13-2) and SUMA2 Network Project - 7th

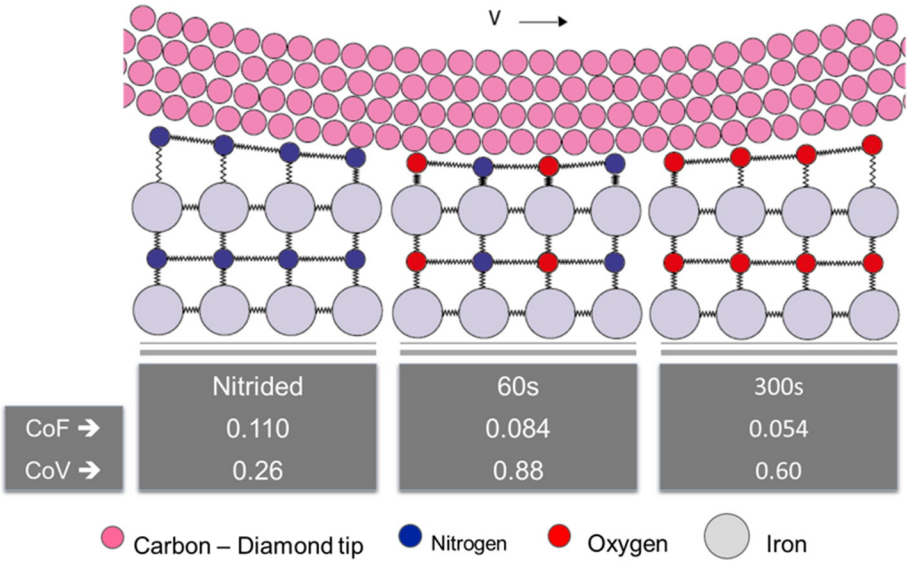

Fig. 7. Schematic of the diamond tip sliding on three different phase distributions. The CoF and CoV are also shown.

Framework Program of the European Commission (IRSES Project # 318903) for their financial support. CMM and NB are CAPES fellows. CAF is CNPq fellow. JB is supported by Erasmus Mundus Programme of the European Commission. C. Menezes and C. Figueroa thank the Material Engineering Center Saarland for all support. The atom probe instrument was financed by the DFG and the Federal State Government of Saarland (INST 256/298-1 FUGG).

References

[1] K. Holmberg, P. Andersson, A. Erdemir, Global energy consumption due to friction in passenger cars, Tribol. Int. 47 (2012) 221.
[2] S.J. Eder, G. Feldbauer, D. Bianchi, U. Cihak-Bayr, G. Betz, A. Vernes, Applicability of macroscopic wear and friction laws on the atomic length scale, Phys. Rev. Lett. 115 (2015) 025502.
[3] B. Wolter, Y. Yoshida, A. Kubetzka, S.-W. Hla, K. von Bergmann, R. Wiesendanger, Spin friction observed on the atomic scale, Phys. Rev. Lett. 109 (2012) 116102.
[4] T.A.L. Burgo, C.A. Silva, L.B.S. Balestrin, F. Galembeck, Friction coefficient dependence on electrostatic tribocharging, Sci. Rep. 3 (2013) 2384.
[5] R.J. Cannara, M.J. Brukman, K. Cimatu, A.V. Sumant, S. Baldelli, R.W. Carpick, Nanoscale friction varied by isotopic shifting of surface vibrational frequencies, Science 318 (2007) 780–783.
[6] J. Krim, Friction and energy dissipation mechanisms in adsorbed molecules and molecularly thin films, Adv. Phys. 61 (2012) 155.
[7] M. Hirano, K. Shinjo, R. Kaneko, Y. Murata, Anisotropy of frictional forces in muscovite mica, Phys. Rev. Lett. 67 (1991) 2642.
[8] R.L.O. Basso, V.L. Pimentel, S. Weber, G. Marcos, T. Czerwiec, I.J.R. Baumvol, C.A. Figueroa, Magnetic and structural properties of ion nitrided stainless steel, J. Appl. Phys. 105 (2009) 124914.
[9] M. Dienwiebel, G.S. Verhoeven, N. Pradeep, J.W.M. Frenken, J.A. Heimberg, H.W. Zandbergen, Superlubricity of graphite, Phys. Rev. Lett. 92 (2004) 126101.
[10] J. Chen, I. Ratera, J.Y. Park, M. Salmeron, Velocity dependence of friction and hydrogen bonding effects, Phys. Rev. Lett. 96 (2006) 236102.
[11] J.Y. Park, M. Salmeron, Fundamental aspects of energy dissipation in friction, Chem. Rev. 114 (2014) 677.
[12] A. Erdemir, S. Li, Y. Jin, Relation of certain quantum chemical parameters to lubrication behavior of solid oxides, Int. J. Mol. Sci. 6 (2005) 203.
[13] M. Freislebem, C.M. Menezes, F. Cemin, F.B. Costi, P.A. Ferreira, C. Aguzzoli, I.J.R. Baumvol, F. Alvarez, C.A. Figueroa, Influence of the chemical surface structure on the nanoscale friction in plasma nitrided and post-oxidized ferrous alloy, Appl. Phys. Lett. 105 (2014) 111603.
[14] O. Joos, C. Boher, C. Vergne, C. Gaspard, T. Nylen, F. Rezaï-Aria, Assesment of oxide scales influence on wear damage of HSM wrok rolls, Wear 263 (2007) 198.
[15] Z. Zhang, X. Lu, J. Liu, Tribological properties of rare earth oxide added Cr_3C_2-NiCr coatings, Appl. Surf. Sci. 253 (2007) 4377.
[16] D.B. Wei, J.X. Huang, A.W. Zhang, Z.Y. Jiang, A.K. Tieu, X. Shi, S.H. Jiao, The effect of oxide scale of stainless steel on friction and surface roughness in hot rolling, Wear 271 (2011) 2417.
[17] A.C. Rovani, A.E. Crespi, V. Sonda, F. Cemin, F.G. Echeverrigaray, C.L.G. Amorim, R.L.O. Basso, I.J.R. Baumvol, C.A. Figueroa, Plasma post-oxidation mechanisms of nitrided ferrous alloys, Surf. Coatings Technol. 205 (2011) 3422.

Please cite this article as: C.M. Menezes, et al., Surf. Coat. Technol. (2016), http://dx.doi.org/10.1016/j.surfcoat.2016.07.095